Title
Tailored Etch Profiles for Wafer-Level Frequency Tuning of Axisymmetric Resonators

Permalink
https://escholarship.org/uc/item/7cw742p7

Journal
Journal of Microelectromechanical Systems, 26(2)

ISSN
1057-7157

Authors
Behbahani, Amir H
Kim, Dennis
Stupar, Philip
et al.

Publication Date
2017-04-01

DOI
10.1109/jmems.2017.2667582

Peer reviewed

Tailored etch profiles for wafer-level frequency tuning of axisymmetric resonators

Amir H. Behbahani, Dennis Kim, Philip Stupar, Jeffrey DeNatale, and Robert T. M'Closkey, *Member, IEEE*

Abstract—This paper reports a wafer-level technique for the systematic elimination of the modal frequency difference between a nominally degenerate pair of modes in an axisymmetric resonator design. A targeted etch process is developed in which masking resist and a conformal layer are ablated at specific sites on the resonator thereby exposing the underlying silicon and enabling site-specific mass removal by SiDRIE. A model of the perturbed resonator dynamics guides the selection of the ablation sites so that the subsequent timed etch reduces the modal frequency differences by a prescribed amount. This wafer-level process is demonstrated on seven resonators whose modal frequency differences are reduced below 100 mHz from initial splits as large as 15 Hz for a pair of modes with 13.5 kHz nominal frequencies.

Index Terms—Gyroscopes, micro-sensors, mode-matched resonators

I. INTRODUCTION

Coriolis vibratory gyros (CVGs) which employ mode-matched resonators have the advantage of maximizing the signal-to-noise ratio of the angular rate measurement relative to noise introduced by signal conditioning electronics. In many cases the resonators are designed with some degree of axisymmetry such that one or more pairs of modes possess nominally degenerate modal frequencies. Small fabrication errors, however, cause the modal frequencies to detune, thereby reducing the signal-to-noise ratio that can be achieved with the associated CVG (see [1] for the analysis of a disk resonator). With the successful development of mode-matched micro-scale disk resonators [2], [3], [4], quadruple mass resonators [5], hemispherical [6], [7], [8], [9], [10], [11], [12], and hemitoroidal [13], [14] resonators, it has become imperative to create post-fabrication corrective procedures so that the pairs of modal frequencies can be brought back to degeneracy. This paper reports the development and application of a wafer-level targeted SiDRIE process for eliminating the modal frequency differences in a planar axisymmetric silicon resonator. The reduction of the frequency difference below 100 mHz is demonstrated for seven resonators on a wafer by selective ablation of masking resist and, in a subsequent step, a conformal layer of Parylene-C such that the mass distribution of the resonator is altered by the removal of silicon at the ablated areas with a timed etch.

A.H. Behbahani and R.T. M'Closkey are with the Mechanical and Aerospace Engineering Department, University of California, Los Angeles.

D. Kim is with ThinKom Solutions, Inc.

P. Stupar and J. DeNatale are with Teledyne Scientific & Imaging, LLC.

R.T. M'Closkey is corresponding author; 38-137 Engineering 4, UCLA, Los Angeles, CA, 90095-1597; ph. 310 825-2909.

There are currently few references reporting the permanent modal frequency mismatch reduction in MEM mode-matched resonators as the current focus is to refine the fabrication processes to yield small initial modal frequency differences prior to any post-fabrication corrective procedures. A notable effort is [7] wherein gold was ablated from the lip of a micro-scale hemispherical resonator in a post-fabrication step. Laser ablation of a ring was also reported in [15] but it degraded the quality factors. The planar resonator design in this paper was also used for modal frequency mismatch reduction by mass-loading the resonator and the resonator frequency models introduced in [3] are further refined in the present paper. One advantage of the present approach over the mass deposition in [3] is the fact that the etch simply removes silicon and does not introduce metals or other material that may not be compatible with downstream processing and packaging. Electrostatic tuning approaches, which do not yield permanent modification of the resonator, are not reviewed here.

The paper is organized as follows. Sec. II-A briefly reviews the resonator used in this study, and Secs. II-B and II-C develop a semi-analytical model of the resonator's $n = 2$ modal frequency difference as a function of mass perturbations. A global sensitivity parameter is also defined and unifies several aspects of the model developed in [3]. Sec. III-A introduces the guided blanket etch, which is the first step in the simultaneous wafer-level reduction of modal frequency differences for individual die. In Secs. III-B and III-C the shortcomings of the guided blanket etch are elucidated and motivate the second step of the tuning process, which involves further targeted etching within each die. The results are discussed in Sec. IV and Sec. V concludes the paper.

II. RESONATOR DESCRIPTION

A. Background

The resonator used in the present work is composed of nine nested rings connected by spokes of varying widths and spacing. There are twenty four large spokes at a given radius which are targets for mass deposition or removal –see Fig. 1. The innermost large spoke layer is designated as the first layer ($i = 1$) and the outermost large spoke layer is designated as the fourth layer ($i = 4$). The resonator is a modification of the design described in [3]. The reader is referred to this paper for information on the resonator fabrication, electrode layout, test procedure, and the process for extracting pertinent modal parameters from empirical frequency response data. In this report the resonator is fabricated without the gold film on, or the reservoirs in, the large spokes. Consequently, these
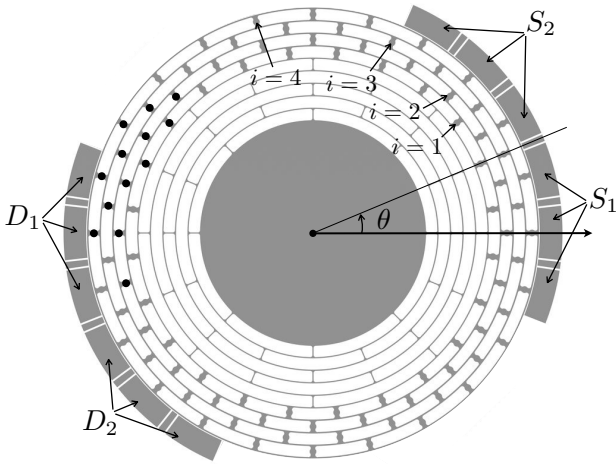
Fig. 1. Electrode arrangement (S is a sense pick-off and D is an electrostatic forcer), angle reference, and spoke layer indices. The dots "•" indicate the locations of perturbations for the finite element case studies.

Fig. 2. Sixteen resonators are fabricated on a 4 inch wafer. Wafer probe of a single resonator also shown.

areas are targets for further etching in order to selectively remove material from the resonator instead of adding material as was pursued in [3]. It will be shown that material removal at the large spokes locations does not modify the stiffness properties of the resonator and so models that readily predict the changes in the resonator modal properties can be developed by assuming only the mass distribution is perturbed. The ultimate goal of this research is the wafer-level production of axisymmetric resonators with degenerate modal frequencies, but in order to make the post-blanket etch processing efficient, improved perturbation models of the resonator are necessary. Thus, the model developed in [3] is further refined in Sec. II-B and applied to the resonators on the 4 inch wafer shown in Fig. 2. Probing of individual resonators is achieved with the card shown in the figure inset or by direct wire bonding between the resonator and a buffer board.

B. Perturbation model

Uniform thin rings possess mode shapes given by $\cos(n\theta)$ and $\sin(n\theta)$ with associated degenerate natural frequencies $\omega_n^2 = \frac{n^6 - 2n^4 + n^2}{n^2 + 1} \frac{EI}{\rho A R^4}$, for $n = 2, 3, 4, \ldots$, where E is the modulus of elasticity, I is the ring cross-section moment of inertia, ρ is the ring material density, A is the ring cross-sectional area, and R is the ring radius. These mode shapes and frequencies are derived from a ring equation of motion that is developed under the same assumptions as those made for an Euler-Bernoulli beam [16]. If the ring is perturbed, however, then, generally speaking, the mode shapes associated with the perturbed frequency ω_n are no longer simply $\cos(n\theta)$ and $\sin(n\theta)$ but will be composed of harmonics of all orders. The mode shapes associated with the resonator considered in this paper are composed of multiple harmonics even for the "ideal" resonator because of the manner in which each ring is attached to its neighbors by the system of spokes, and despite the fact that the 2θ harmonics have the largest amplitude for ω_2 (the $n = 2$ wine glass modes), it is necessary to quantify other dominant harmonics in order to build an accurate model of the spoke velocities.
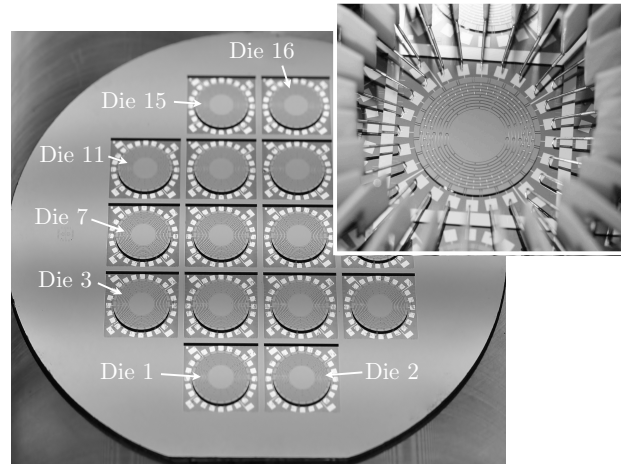
Due to the complexity of the resonator design a semi-analytical approach is adopted in order to develop a perturbation model for the resonator dynamics. As in [3], the natural frequency deviation due to perturbations at the large spokes is modeled as a change in the resonator kinetic energy only –the elastic strain energy remains constant under these perturbations. This assumption is supported by finite element analysis. For example, Fig. 3 shows the strain energy density on a portion of the resonator for an $n = 2$ mode. The dark vertical bands on the side walls at the root of the spokes are the areas with the largest strain energy density while the white areas are where strain energy is smallest. Since the center of the spokes themselves have very little strain energy, selective etching these areas is assumed to only modify the kinetic energy of the modes.

The analysis of the perturbed kinetic energy of a given mode due to a small change in mass at the large spokes requires the radial and tangential components of the in-plane velocities at the large spokes. These velocity components can be represented as a discrete Fourier series with twelve distinct spatial harmonics since there are twenty four spokes in a given layer. It will be shown that the ratios of the *amplitudes* of these harmonics can be assumed to be independent of the intensities and location of the mass perturbations. In other words, it is assumed that the mass perturbations are sufficiently small so that the relative amplitudes of the harmonics present in a given mode are not modified by the presence of the mass perturbations. This assumption is supported by the numerical case studies reported in Sec. II-C. On the other hand, the spatial orientations (phases) are dependent on the mass perturbations. For a given mode of the $n = 2$ pair, denoted with index $p \in \{1, 2\}$, the radial and tangential velocities at particular spoke, defined by angle θ and spoke layer $i \in \{1, 2, 3, 4\}$, can be represented by the following partial Fourier series

$$U_{p,i}(\theta) = \sum_{k=2,6,10} \alpha_{i,k} \cos(k(\theta - \psi_{p,k})),$$
$$W_{p,i}(\theta) = \beta_{i,2} \sin(2(\theta - \psi_{p,2})),$$

(1)

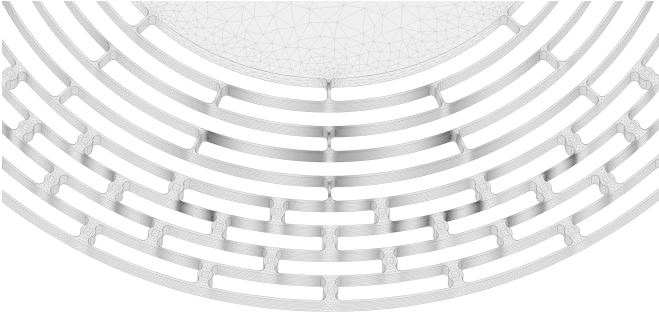where the index k defines the $k\theta$ harmonic of the $n = 2$

Fig. 3. Detail of meshed resonator showing the large spokes. The dark vertical bands on the sidewalls are the areas where the strain energy density is highest.

mode shape, and $U_{p,i}$ and $W_{p,i}$ represent the radial and tangential velocity components, respectively. The amplitudes of the harmonics are represented by $\alpha_{i,k}$ and $\beta_{i,2}$ for the radial and tangential velocities, respectively, and the phases of the harmonics are represented by $\psi_{p,k}$. It should be noted that (1) is specific for the resonator design under consideration and that other axisymmetric designs may possess a different set of dominant harmonics in the mode shapes. At the very least, $\alpha_{i,k}$ and $\beta_{i,k}$ will differ across resonator designs, however, Sec. II-C outlines a procedure that can be used to identify the important harmonics and associated parameters.

The form of (1) requires that the following be justified: 1) only three spatial harmonics are required to represent a spoke's radial velocity component ($k \in \{2, 6, 10\}$), 2) only one harmonic is required to represent a spoke's tangential velocity ($k = 2$), 3) the amplitudes of the harmonics are independent of θ and $n = 2$ mode under consideration (the amplitudes only depend on the layer, i, and harmonic index, k), 4) the phases $\psi_{p,k}$ depend on the mode and harmonic indices, but not the layer, and 5) the radial and tangential components have the same $k = 2$ phase. The justification is postponed until Sec. II-C so that an expression for the post-perturbation change in the differences of the modal frequencies can be developed.

A single mass perturbation of value m_0 (may be negative if mass is removed) located on the ith layer at angle θ_0 creates the following perturbations to the kinetic energies of each $n = 2$ mode,

$$T_p = \frac{1}{2} m_0 \left(U_{p,i}^2(\theta_0) + W_{p,i}^2(\theta_0) \right), \quad p = 1, 2. \qquad (2)$$

The out-of-plane velocity is negligible for the $n = 2$ modes and is ignored in this analysis. The Rayleigh-Ritz method is used to estimate the perturbation of a modal frequency due to a perturbation of the resonator kinetic energy [17]. Consequently, the mass perturbation perturbs each modal frequency according to

$$\omega_1^2 = \omega_{1,0}^2 \frac{1}{1 + \epsilon_1} \approx \omega_{1,0}^2 \left(1 - \epsilon_1 \right),$$
$$\omega_2^2 = \omega_{2,0}^2 \frac{1}{1 + \epsilon_2} \approx \omega_{2,0}^2 \left(1 - \epsilon_2 \right), \qquad (3)$$

where $\omega_{1,0}$ and ω_1 are the pre- and post-perturbation natural frequencies of one of the $n = 2$ modes, respectively, and $\omega_{2,0}$

and ω_2 are the pre- and post-perturbation natural frequencies of the second companion $n = 2$ mode. The relative change in kinetic energies of the modes due to the perturbation are denoted ϵ_1 and ϵ_2 and are equal to $T_1/T_{1,0}$ and $T_2/T_{2,0}$, where $T_{1,0}$ and $T_{2,0}$ are the nominal kinetic energies in each mode prior to the perturbation. It is necessary for $T_1 << T_{1,0}$ and $T_2 << T_{2,0}$ in order for these approximate expressions to be accurate, however, this requirement is satisfied in practice since the absolute change in a given modal frequency is typically less than one part in a thousand.

The mass perturbations are selected to reduce the difference in perturbed modal frequencies so it is useful to manipulate the expressions in (3) such that the difference is explicit,

$$\omega_2^2 - \omega_1^2 = \omega_{2,0}^2 - \omega_{1,0}^2 - \omega_{2,0}^2 \epsilon_2 + \omega_{1,0}^2 \epsilon_1. \qquad (4)$$

Terms can be factored: $\omega_2^2 - \omega_1^2 = (\omega_2 - \omega_1)(\omega_2 + \omega_1)$ and $\omega_{2,0}^2 - \omega_{1,0}^2 = (\omega_{2,0} - \omega_{1,0})(\omega_{2,0} + \omega_{1,0})$. The expressions of interest are the pre- and post-perturbation differences in the modal frequencies. The pre-perturbation difference is denoted $\Delta_0 := \omega_{2,0} - \omega_{1,0}$ and the post-perturbation difference is denoted $\Delta := \omega_2 - \omega_1$, thus, (4) is rearranged to

$$\Delta = \Delta_0 \frac{\omega_{2,0} + \omega_{1,0}}{\omega_2 + \omega_1} - \frac{\omega_{2,0}^2}{\omega_2 + \omega_1} \epsilon_2 + \frac{\omega_{1,0}^2}{\omega_2 + \omega_1} \epsilon_1. \qquad (5)$$

Let ω_0 represent the average modal frequency of the $n = 2$ modes for the resonator under consideration, then, the leading order value of the ratio $(\omega_{2,0} + \omega_{1,0})/(\omega_2 + \omega_1)$ is 1 and the leading order value for the ratios $\omega_{2,0}^2/(\omega_2 + \omega_1)$ and $\omega_{1,0}^2/(\omega_2 + \omega_1)$ is $\omega_0/2$. Thus, the following relation approximately relates the pre- and post-perturbation values of the frequency difference,

$$\Delta = \Delta_0 - \frac{\omega_0}{2} \left(\frac{T_2}{T_{2,0}} - \frac{T_1}{T_{1,0}} \right). \qquad (6)$$

Substituting (2) into (6) yields an expression relating the pre- and post-perturbation modal frequency *differences* due to a mass perturbation of size m_0 located on the ith layer at angle θ_0

$$
\begin{aligned}
\Delta = \Delta_0 &- \frac{\omega_0 m_0 \alpha_{1,2}^2}{4 T_{2,0}} \left[\left(\sum_k \tilde{\alpha}_{i,k} \cos(k(\theta_0 - \psi_{2,k})) \right)^2 \right. \\
&\left. + \left(\tilde{\beta}_{i,2} \sin\left(2(\theta_0 - \psi_{2,2})\right) \right)^2 \right] \\
&+ \frac{\omega_0 m_0 \alpha_{1,2}^2}{4 T_{1,0}} \left[\left(\sum_k \tilde{\alpha}_{i,k} \cos(k(\theta_0 - \psi_{1,k})) \right)^2 \right. \\
&\left. + \left(\tilde{\beta}_{i,2} \sin(2(\theta_0 - \psi_{1,2})) \right)^2 \right],
\end{aligned}
\qquad (7)
$$

where k is summed over indices $\{2, 6, 10\}$. In this expression the radial harmonic amplitude for $k = 2$ and $i = 1$, i.e. $\alpha_{1,2}$, is factored out of the kinetic energy expressions and is used to normalize the remaining amplitudes. In other words, $\tilde{\alpha}_{i,k} := \alpha_{i,k}/\alpha_{1,2}$ and $\tilde{\beta}_{i,2} = \beta_{i,2}/\alpha_{1,2}$. It will be shown in Sec. II-C that these normalized amplitudes can be assumed to be independent of the mode under consideration and independent of the size of the (small) mass perturbation. The fact that

$\tilde{\alpha}_{i,k}$ and $\tilde{\beta}_{i,2}$ are the same for both $n = 2$ modes, and the fact that they are independent of the mass perturbation, implies that the kinetic energy in a given mode is determined by specifying any one of the harmonic amplitudes. In this analysis, it is convenient to specify $\alpha_{1,2}$, which is why it is factored out of the expressions in (7). Thus, further consolidation in (7) is possible because $\alpha_{1,2}^2/T_{1,0} = \alpha_{1,2}^2/T_{2,0}$. These ratios are denoted by the parameter α_T. Thus, the constant multiplying the sums with the normalized velocity components is defined as the *resonator sensitivity parameter*, denoted γ,

$$\gamma = \frac{1}{4}\omega_0 m_0 \alpha_T. \tag{8}$$

This single global sensitivity parameter represents, in a general sense, the change in the modal frequency difference for a mass perturbation of value m_0 (the unit of γ is rad/s). It will be numerically estimated in Sec. II-C and experimentally estimated in Sec. III-B. Note that γ can be used for all resonators of a specific design, i.e. it is not necessary to measure the parameter for each resonator. This definition also removes a shortcoming of the model developed in [3] which required the estimation of a separate sensitivity parameter for each layer of spokes. The unified treatment also eases test requirements because the mass perturbations need not be located on the anti-nodes, which was the case for the sensitivity parameters described in [3].

Multiple mass perturbations can be addressed by extending (7). In fact, the effect of simultaneous perturbations on the modal frequency difference are additive because the perturbed kinetic energies of the modes are simply a sum of the individual perturbations, i.e. these terms are added to (2). Thus, if there are l mass perturbations, located at angles θ_q, $q = 1, 2, \ldots, l$, and spoke layer $i_q \in \{1, 2, 3, 4\}$ with mass $r_q m_0$, where r_q represents the mass perturbation relative to m_0, then the expression for Δ is

$$\Delta = \Delta_0 - \gamma \sum_{q=1}^{l} r_q \Bigg[\left(\sum_k \tilde{\alpha}_{i_q,k} \cos(k(\theta_q - \psi_{2,k})) \right)^2 \\ + \left(\tilde{\beta}_{i_q,2} \sin\left(2(\theta_q - \psi_{2,2})\right) \right)^2 \\ - \left(\sum_k \tilde{\alpha}_{i_q,k} \cos(k(\theta_q - \psi_{1,k})) \right)^2 \\ - \left(\tilde{\beta}_{i_q,2} \sin(2(\theta_q - \psi_{1,2})) \right)^2 \Bigg]. \tag{9}$$

It is worthwhile reviewing what information is required to use (9) in order to predict Δ. First, Δ_0 is estimated from frequency response measurements of the resonator prior to the mass perturbation using the modeling process described in [3]. The normalized radial and tangential velocity amplitudes are determined from finite element analysis (FEA) in Sec. II-C and yield a numerical estimate of γ (a series of experiments in Sec. III-B provide an experimental estimate). Finally, the phases of the harmonics, $\psi_{p,k}$, must be considered. The phases must be experimentally determined because they will be different for every fabricated resonator and will change after a perturbation cycle. This analysis provides insight into what should be measured for employing a comprehensive

model of the frequency perturbation as a function of the mass perturbation. For the resonator design under consideration, however, it is only possible to reliably measure the phase of the $k = 2$ harmonic. This is discussed in more detail in Sec. III.

C. Numerical case studies

This section provides numerical justification for the assumptions that were invoked in claiming (1) is a reasonable model for the spoke velocities. Since the resonator dynamics are difficult to quantitatively analyze using a first principles approach, modal analysis of the structure using finite elements is used to compute the radial and tangential velocity components at all large spokes. The finite element model is not fit to a given empirical frequency response as this would be a time consuming and ultimately fruitless pursuit since it is not known how to estimate the local variations in mass and stiffness that produce the observed deviations from a modally degenerate "ideal" resonator. Thus, the modal analysis is used to identify features in the modes which appear to be invariant under small perturbations.

An example of the fine mesh that is used in the FEA is shown in Fig. 3. The modal analysis yields the Cartesian velocity components at any point in the resonator but because mass is removed from the large spokes in the physical resonators, the spoke velocity components are of particular interest. For the FEA study, the mass at the large spokes is manipulated by changing the density of the elements in an $80\mu\text{m} \times 80\mu\text{m}$ patch in the center of the spokes (also shown in Fig. 3), Thus, the Cartesian velocity components are determined at the center of each large spoke on the top surface of the resonator and then transformed into radial and tangential components. Then, the discrete Fourier series of the radial and tangential components are computed for each spoke layer (24 spokes per layer). Each perturbation "experiment," in which the density of the square patch is varied, yields Fourier series for the velocity components for each mode. A total of twenty four perturbation case studies were performed: there are thirteen single spoke perturbations at the locations shown in Fig. 1. In addition to the single spoke perturbations, multi-mass perturbations involving pairs of spokes were also conducted. The modal analysis shows that the *ratios* of the amplitudes of Fourier series coefficients for the radial and tangential velocity components can be assumed to be constant and independent of the $n = 2$ mode under consideration, even when the resonator is perturbed.

The results of all twenty four case studies are summarized in Fig. 4. The largest magnitude Fourier coefficient in all cases corresponds to $\alpha_{1,2}$, that is, the $k = 2$ harmonic in the radial velocity at the innermost spoke layer ($i = 1$). All other Fourier coefficient magnitudes in each experiment are normalized by $\alpha_{1,2}$ to yield the normalized Fourier coefficient magnitudes (denoted $\tilde{\alpha}$ and $\tilde{\beta}$) shown in this figure. The following may be concluded from Fig. 4: 1) only the $k \in \{2, 6, 10\}$ terms of radial velocity harmonics, and $k = 2$ term for the tangential velocity harmonics, need to be retained for an accurate description of the spoke velocities due to the fact that these Fourier components are dominant, 2) for a given i and k,
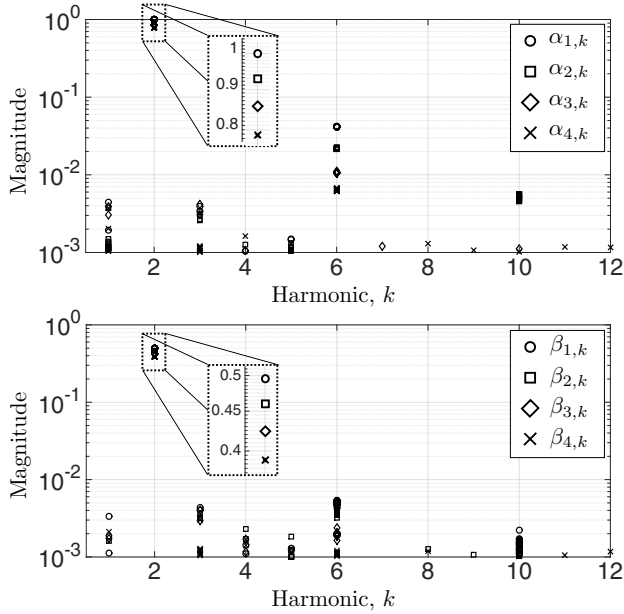
Fig. 4. (Top) The magnitude of the Fourier series coefficients for the spoke radial velocities at different layers. All the harmonics are negligible except for $k \in \{2, 6, 10\}$. (Bottom) The magnitude of the Fourier series coefficients for the spoke tangential velocities. All harmonics are negligible except for $k = 2$.

the normalized amplitudes are the same for each mode in the $n = 2$ pair, and 3) the normalized amplitudes can be assumed to be *independent* of the mass perturbation intensity and location due to the clustering of normalized amplitudes for a given harmonic and spoke layer. The values of the normalized amplitudes that are retained for the analysis are summarized in Table I. It can be argued that retaining the $k = 1, 3$ radial velocity harmonics is justified due to their amplitude relative to $k = 10$, however, due to the limited sensing in the present resonators, it is not possible to measure all of the harmonic phases necessary for predicting the post-perturbation frequency difference so these terms are neglected in the analysis.

The phases associated with the Fourier series must also be addressed. The Fourier analysis has treated each spoke layer separately, however, the numerical experiments show that for a given test case, the phases for each harmonic are the same for all spoke layers. This vastly simplifies the analysis because all the layers will have the same pattern of motion with different amplitudes only. This is the reason that the frequency perturbation model (7) assumes for a given harmonic, that the phases of each layer are equal. This property is appealing because it means that it is necessary to measure the phase of only one spoke layer when determining the phase of the $k\theta$ harmonic. Numerical evidence supports this hypothesis. For this part of the discussion, the notation will be modified in order to avoid a proliferation of indices. The phase of a particular harmonic is still denoted by ψ, however, the subscript will now indicate the particular spoke layer. The mean value of the set of phase differentials across layers $\{\psi_4 - \psi_3, \psi_4 - \psi_2, \psi_4 - \psi_1\}$ for the radial $k = 2$ harmonic, considering both $n = 2$ modes, and then averaging over the

entire set of numerical cases is $-0.0042°$ with a standard deviation of $0.0123°$. The same computation for the radial $k = 6$ harmonic yields a mean value of $0.5326°$ with standard deviation of $0.2930°$. Finally, for the $k = 10$ harmonic, the mean value of $\psi_2 - \psi_1$ is $0.5117°$ with a standard deviation of $0.4582°$. These results justify the form for the radial velocity $U_{p,i}$ in (1) in which the phases are independent of the ring under consideration.

The phases of Fourier series coefficients for the spoke tangential velocities must be studied in order to justify the representation of $W_{p,i}$ in (1). Only the $k = 2$ harmonic is significant in the Fourier series of the tangential velocities according to Fig. 4. The mean value of the set of phase differentials across layers $\{\psi_4 - \psi_3, \psi_4 - \psi_2, \psi_4 - \psi_1\}$ for the tangential $k = 2$ harmonic, considering both $n = 2$ modes, and averaged over the set of numerical cases is $-0.0066°$ with a standard deviation of $0.0250°$. This implies that the phase of the $k = 2$ tangential harmonics are equal across the spoke layers. Furthermore, for a given $n = 2$ mode, computation of the phase difference between the $k = 2$ harmonics for the radial and tangential velocities is $45.00°$ with a standard deviation of $0.0194°$, which implies the phases are locked. In other words, measurement of the $k = 2$ phase associated with the radial velocity also determines the phase associated with the tangential velocity. This analysis is required to justify (1) since the $45°$ phase difference between the tangential velocities and radial velocities is accommodated by using the sine function in $W_{p,i}$ instead of cosine function with the $45°$ offset. It is interesting to note that for a thin, uniform, inextensible ring the kinematic relationship $U = dW/d\theta$ exists between the in-plane radial and tangential velocities, which implies the phases of the $k = 2$ radial and tangential velocity harmonics differ by $45°$ [16].

Additional information can be extracted from the finite element analysis of the perturbation cases. Considering a single test case, the phase difference between each mode for a given harmonic can be computed and then these values can be averaged over all test cases. Using the same phase notation as (1), the following is determined for each test case: $\psi_{2,k} - \psi_{1,k}$, separately for $k = 2, 6, 10$. Averaging over all test cases yields a value of $44.9954°$ for $k = 2$ with a standard deviation of $0.0125°$, $15.0200°$ for $k = 6$ with a standard deviation of $0.6451°$, and $9.0038°$ for $k = 10$ with a standard deviation of $0.0414°$. This shows that the $k\theta$ harmonics of the two $n = 2$ modes in a given test case can be assumed to be spatially orthogonal in the sense that $|\psi_{2,k} - \psi_{1,k}| = 90°/k$. The velocity components (1) do not make explicit use of this property because it is assumed that $\psi_{p,k}$ are available from measurements, however, this property will be assumed when using (9) to compute a range for Δ for a given perturbation scenario due to unmeasured phases. Finally, the FEA is also estimate the sensitivity parameter

$$\gamma_{\text{FEA}} = 0.325 \, \text{Hz} \qquad (10)$$

for a mass of $m_0 = 0.1193 \, \mu g$. This mass is equivalent to an $80 \, \mu m \times 80 \, \mu m \times 8 \, \mu m$ rectangular prism of silicon which corresponds to a nominal amount of silicon to be removed in the experiments in Sec. III-B.

TABLE I
NORMALIZED AMPLITUDES OF VELOCITY HARMONICS (STANDARD
DEVIATION IN PARENTHESIS)

layer, i	$\tilde{\alpha}_{i,2}$	$\tilde{\alpha}_{i,6}$	$\tilde{\alpha}_{i,10}$	$\tilde{\beta}_{i,2}$
1	1	0.0413	0.0287	0.4969
	(0)	(0.00021)	(0.00015)	(0.00031)
2	0.9289	0.0218	0.0055	0.4603
	(0.00011)	(0.00023)	(0.00040)	(0.00036)
3	0.8506	0.0107	0	0.4214
	(0.00034)	(0.000071)	($\star$)	(0.00010)
4	0.7868	0.0065	0	0.3886
	(0.00013)	(0.00020)	($\star$)	(0.00025)

TABLE II
SUMMARY OF STANDARD BLANKET ETCH RESULTS

Die	ω_1 (Hz)	ω_2 (Hz)	Δ_0 (Hz)
1	13394.90	13407.03	12.13
3	13285.87	13298.98	13.11
4	**13508.92**	**13520.46**	**11.54**
5	13592.69	13603.21	10.52
6	13594.35	13609.33	14.98
7	13306.43	13333.70	27.27
9	13657.04	13670.67	13.63
10	13640.40	13652.94	12.54
11	13110.13	13124.30	14.17
12	**13365.44**	**13377.51**	**12.07**
14	**13543.59**	**13554.77**	**11.18**
15	13056.97	13070.67	13.70
16	**13197.65**	**13213.42**	**15.77**

III. WAFER-SCALE FREQUENCY TUNING

The targeted etch approach for reducing the frequency split across all resonators proceeds in two steps. The first step, after the standard blanket etch concludes, is to ablate photoresist on the resonators in strategic areas so that continued etching will reduce the $n = 2$ modal frequency differences to a greater degree than the standard blanket etch alone. The perturbation model developed in Sec. II-B is used to select ablation locations, however, it is shown that it is not possible to fine-tune the modal frequencies since etching with small areas exposed on the spokes (denoted the *guided blanket etch*) will still globally etch the resonator and modify its dynamics in a manner that is not predicted by the perturbation model. Indeed, the test results in Sec. III-A suggest that the mass removal modifies the stiffness and mass distribution of the resonator in a complicated and unpredictable manner. The second step of targeted etching occurs once the photoresist is stripped from the wafer and a conformal coat of Parylene-C is applied. The coating is then ablated in desired areas and a timed etch commences, but because the conformal coat withstands the etch, only the exposed areas have material removed and the perturbation model in this case accurately predicts the post-etch modal frequency difference. Thus, the model can be used as a guide for selecting the areas for conformal coat ablation. The second step is discussed in Sec. III-C.

A. Guided blanket etch

At the conclusion of the standard blanket etch, there is an opportunity to selectively remove material from the large spokes by ablating the photoresist and continuing the etch. It is necessary to estimate the modal parameters in order to use (7) to search for ablation locations such that Δ is reduced to the desired level. As only one wafer was available for experimentation, the sensitivity parameter γ was estimated from the FEA (see (10)), although experimental estimates of γ are obtained later. The limited sensing in the resonator (the radial velocity for the outermost ring is measured by electrodes that subtend a $15°$ arc, [3]) means that it is not possible to reliably measure $\psi_{p,6}$ and $\psi_{p,10}$ because the normalized amplitudes associated with the outermost spokes ($i = 4$) is about two orders of magnitude smaller than the amplitudes of the $k = 2$ harmonics. Furthermore, the spatial filtering of the electrodes further reduces the gain of these harmonics. The

ideal locations in the resonator for measuring $\psi_{p,6}$ and $\psi_{p,10}$ are in the innermost spoke layers ($i = 1$) where electrodes do not currently exist for measuring the in-plane motion. The perturbation model (9) is truncated to include only the $k = 2$ harmonics for purposes of selecting the ablation sites. In other words, the following expression is used to search over θ and i to determine suitable locations for perturbations that will reduce $|\Delta|$ below a desired value,

$$
\begin{aligned}
\Delta = \Delta_0 - \gamma \sum_{q=1}^{l} r_q \Big[& \tilde{\alpha}_{i_q,2}^2 \cos^2(2(\theta_q - \psi_{2,2})) \\
& + \tilde{\beta}_{i_q,2}^2 \sin^2\left(2(\theta_q - \psi_{2,2})\right) \\
& - \tilde{\alpha}_{i_q,2}^2 \cos^2\left(2(\theta_q - \psi_{1,2})\right) \\
& - \tilde{\beta}_{i_q,2}^2 \sin^2(2(\theta_q - \psi_{1,2})) \Big].
\end{aligned}
\tag{11}
$$

Nevertheless, (9) will be used to estimate upper and lower bounds for Δ by assuming worst-case values for the unmeasured phases $\psi_{p,6}$ and $\psi_{p,10}$.

The modal parameters of each resonator on the 16-die wafer (Fig. 2) can be estimated after the standard blanket etch concludes even with the photoresist present. The photoresist mass-loads the resonator and dampens the modes, however, reliable estimates of the modal frequency *difference*, i.e. Δ_0, and the $k = 2$ phases can be obtained. The measured modal frequencies are summarized in Table II. Die 2, 8, and 13 are non-functional and are not included in the table. The $n = 2$ modal frequencies extend from 13.057 kHz to 13.657 kHz and the modal frequencies differences extend from 10.52 Hz to 27.27 Hz. This range of mean frequencies and initial differences suggests that each die will require a custom etch profile. The modal frequency differences reported here are always positive because ω_2 is always assigned to higher frequency $n = 2$ mode once the measurements have been made. Thus, the phase $\psi_{2,2}$ in (11) is associated with the higher frequency mode as well. It is possible that the models (9) and (11) will predict $\Delta < 0$, however, if a subsequent cycle of etching is desired, then the labels on the modes will be switched along with their corresponding phases.

The spokes that are selected for ablation are determined by searching over a handful of ablation sites in a neighborhood of
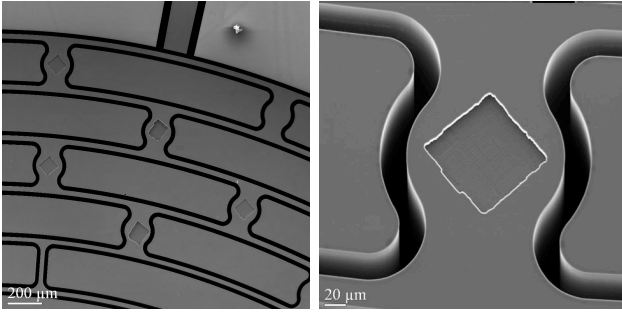
Fig. 5. Etched areas on resonator after Parylene ablation.

TABLE III
SUMMARY OF GUIDED BLANKET ETCH RESULTS

Die	ω_1 (Hz)	ω_2 (Hz)	Q_1 (k)	Q_2 (k)	Δ (Hz)
1	13327.14	13329.49	47.0	47.2	2.35
3	13239.00	13242.99	48.7	48.6	3.99
4	**13465.70**	**13474.78**	**45.9**	**46.0**	**9.08**
5	13554.99	13556.51	46.7	42.8	1.52
6	13557.38	13560.13	46.7	46.9	2.75
7	13231.85	13248.81	46.0	48.1	16.96
9	13613.48	13615.77	40.9	42.4	2.29
10	13592.83	13594.45	46.3	46.4	1.62
11	12979.60	12982.25	44.4	50.3	2.65
12	**13282.89**	**13291.49**	**47.9**	**48.2**	**8.60**
14	**13467.45**	**13475.62**	**47.4**	**47.4**	**8.17**
15	12943.30	12944.95	47.9	50.8	1.65
16	**13063.30**	**13074.64**	**46.2**	**49.5**	**11.34**

the lower frequency mode anti-nodes such that a reduction of the frequency differences of approximately 8 Hz is achieved for all resonators as predicted by (11), i.e. due to the large spread in Δ_0, the guided blanket etch is designed to achieve $\Delta - \Delta_0 \leq 8$ Hz. Die 4, 12, 14 and 16 are used for experimental controls and are not ablated. In other words, these die will continue to be etched using the standard process, while the ablated resonators will experience the targeted etch at the spokes in addition to the standard process. The ablation is performed using a New Wave Research QuikLaze laser cutting system. The ablated areas are approximately 80 μm by 80 μm. A DRIE timed etch is performed such that the modal frequency difference would be reduced by 8 Hz in the absence of any other factors that could influence the modal frequencies. The etch time is defined by the desired etch depth to remove the targeted mass of material. Using a calibrated etch rate, the corresponding time is calculated. Due to the large size of the ablated features and the short etch depths, etch rate consistency run-to-run is typically within a few percent. The sensitivity parameter γ_{FEA} is used to estimate the duration of the timed etch based on the desired etch depth. The results of the guided blanket etch are shown in Table III and it is clear that the ablated die experience greater reductions in modal frequency differences compared to the control die. Fig. 5 shows a resonator with trimmed spoke (after Parylene ablation and etch). Figs. 6 and 7 show empirical frequency responses of two measurement channels for Die 14 (a control die) and Die 3, respectively, before and after the guided blanket etch. In Table III, the modal parameter measurements were made after the photoresist was stripped so that accurate damping values are obtained. Note that continuing the blanket etch on the control die further reduces the modal frequency differences. The reductions range from 2.5 to 4.4 Hz depending on the die, but it illustrates the unfeasibility of using the blanket etch to eliminate the frequency differences across all die, especially since the range of starting Δ_0 is large. Note, however, that the ablated die all experience significant reductions in their modal frequency differences but the variability introduced from etching other areas of the resonator still creates too much uncertainty to accurately predict the final modal frequency difference. Nevertheless, this exercise demonstrates that the guided blanket etch can be used to systematically reduce Δ and provide a good starting point for the targeted etching that follows.
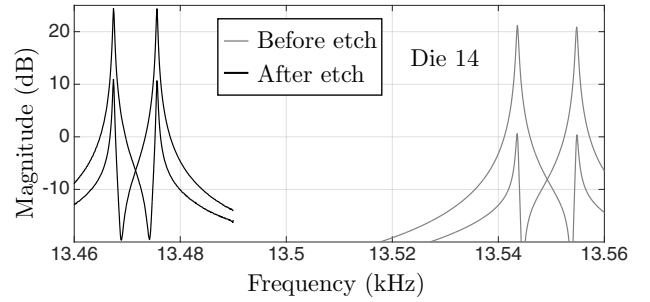

Fig. 6. Mean modal frequencies reduce with further blanket etching. The modal frequency difference also has a modest reduction.

B. Sensitivity parameter measurements

A coating of Parylene C, approximately 1 μm in thickness, is applied to the wafer at the conclusion of the guided blanket etch. The Parylene protects the resonator from further etching unless the laser is used to expose the underlying silicon. Parylene was selected based on the ease of ablating the material without damaging the underlying silicon, and on its conformality, which protects the sidewalls of the structure during the etch in addition to the top surface. This sidewall coating prevents lateral etching, which impacts the width (and hence stiffness) of the device. In addition, the Parylene is deposited using a vapor-deposition process, avoiding wet processing, and it can be cleanly removed using an oxygen
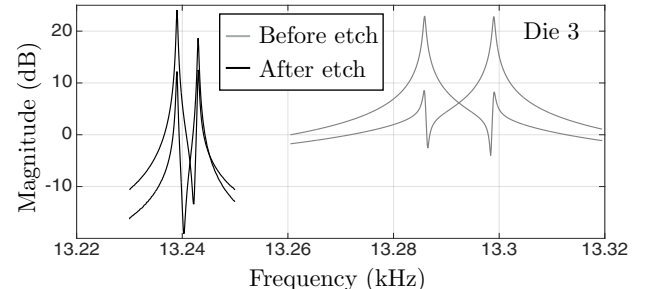

Fig. 7. Modal frequencies after photoresist ablation on selected spokes and further blanket etching experiences larger reduction in frequency difference.

TABLE IV
SUMMARY OF SENSITIVITY PARAMETER ESTIMATES

Die	round	layer, i	Δ_0 (Hz)	Δ (Hz)	r_m	γ (Hz)
4	1	3	9.08	8.16	-1.2661	0.3334
4	2	1	8.16	7.08	-1.0200	0.3526
4	3	2	7.08	6.20	-1.0105	0.3724
4	4	4	6.20	5.69	-0.9654	0.3295
12	1	2	8.60	7.69	-1.1579	0.3643
12	2	4	7.69	7.18	-1.0196	0.3453
12	3	1	7.18	6.10	-1.0541	0.3484
12	4	3	6.10	5.33	-1.0279	0.3534
14	1	4	8.17	7.39	-1.2352	0.3438
14	2	2	7.39	6.29	-1.2798	0.3379
14	3	3	6.29	5.63	-0.9766	0.3214
14	4	1	5.63	4.67	-0.9858	0.3428
16	1	1	11.34	10.15	-1.1542	0.3431
16	2	3	10.15	9.33	-1.0689	0.3526
16	3	4	9.33	8.74	-1.0276	0.3369
16	4	2	8.74	7.88	-1.0160	0.3636

TABLE V
MODAL PARAMETERS ASSOCIATED WITH NON-ABLATED DIE

	Before Etch		After Etch	
Die	Mean ω (Hz)	Δ (Hz)	Mean ω (Hz)	Δ (Hz)
3	13241.00	3.99	13241.80	4.01
5	13555.75	1.52	13555.70	1.60
11	12980.92	2.65	12981.45	2.66
15	12944.12	1.65	12944.35	1.70

The sensitivity parameter experiments also provide an opportunity to determine to what extent the modal properties of non-ablated die have changed. Measurements were made on the four die shown in Table V and demonstrate that the Parylene prevents material removal over the short duration of the timed etch. The mean frequencies are reported along with the modal frequency difference before and after the etch. The mean frequencies can vary due to small fluctuations in wafer temperature (the wafer is not temperature regulated during the tests). Furthermore, the small differences in pre- and post-etch Δ are within the accuracy of the model that is fit to the frequency response data and from which the modal parameters are extracted.

C. Wafer-level elimination of modal frequency differences

The sensitivity parameter experiments were conducted using Die 4, 12, 14 and 16 to provide an estimate of γ but it is evident in Table IV that the ablation locations were also selected so as to reduce Δ, although not to a specified target. Now the objective is to use γ_{EXP} and (11) to select ablation locations on the complementary "test" die in order to achieve $\Delta \approx 0$ for these die. Several Parylene deposition-ablate-etch-measure cycles were performed with the wafer because of the approximate nature of (11) in predicting the post-etch frequency difference, however, during each cycle all test die were modified in order to demonstrate the feasibility of *simultaneously* reducing Δ across all die on the wafer. Between each cycle, the Parylene is removed with an oxygen plasma etch. In order to achieve the simultaneous reduction of Δ, it is necessary to ablate areas of differing sizes on the spoke surfaces so as to customize the material removal for each die since each round of etching penetrates the same depth for all die (typically about 8 μm). For these experiments areas of dimensions 22μm $\times$ 22μm to 87μm $\times$ 87μm were ablated. The model (11) includes the scaling r_q to account for the deviation of the expected material removal with respect to the mass m_0. The final results are compiled in Table VI. All modal frequency differences are reduced below 100 mHz with the exception of Die 3 and 7, the latter of which was used for continued sensitivity parameter experiments. The success of this approach is easily seen in Figs. 8 and 9, which show the empirical frequency responses of each test die (with the exception of Die 7) before and after the targeted etch process.

plasma.

The initial objective is to experimentally estimate γ from a series of tests on the control Die 4, 12, 14 and 16. Four rounds of experiments are conducted on these die in which four square patches, approximately 80 μm $\times$ 80 μm, are opened on a selected spoke layer in a compass-points pattern. A timed etch removes approximately 8 μm of material from these areas for each round of experiments. A single round targets different spoke layers on the different die. For example, in the first round, Die 4 has material removed from the third spoke layer, but Die 12 has material removed from the second spoke layer. The results of the experiments are collected in Table IV. The volume that is associated with γ is $80 \times 80 \times 8$ μm^3, which corresponds to a mass of $m_0 = 0.1193\,\mu$g. At the conclusion of each round of etching, the modal parameters are measured and precise dimensions of the material removed are obtained with a Wyko profilometer. Then, the parameter r_m is determined which relates the actual mass perturbation estimated from the Wyko measurements relative to the canonical mass m_0. The fact that $r_m < 0$ indicates that material has been removed, and if $|r_m| > 1$, then more mass was removed than the mass m_0. The sensitivity parameter is then estimated from (11), where γ is replaced by $r_m\gamma$. Note that Δ, Δ_0, $\psi_{2,2}$ and $\psi_{1,2}$ are known from the pre- and post-etch modal parameter measurements, θ_0 and index i are defined by the etched spoke locations, and $\tilde{\alpha}_{i,2}$ and $\tilde{\beta}_{i,2}$ are known from the FEA. Thus, the estimated γ is calculated for each round and reported in Table IV. The estimates with the lowest variance correspond to spoke layer $i = 4$, i.e. the outermost layer of spokes. This can be attributed to the fact that the neglected $k = 6, 10$ harmonics in (11) have little effect on the spoke velocities in this layer. Thus, the mean value obtained from perturbations to the outermost spoke layer are used for the estimate of

$$\gamma_{\text{EXP}} = 0.339\,\text{Hz}. \qquad (12)$$

Note that the estimates from the other spoke layers are very close to this value as is the value for γ_{FEA}.

IV. DISCUSSION

Tailored etching using the Parylene deposition-ablation-etch cycle appears to be successful in reducing modal frequency

TABLE VI
SUMMARY OF PARYLENE ETCH RESULTS

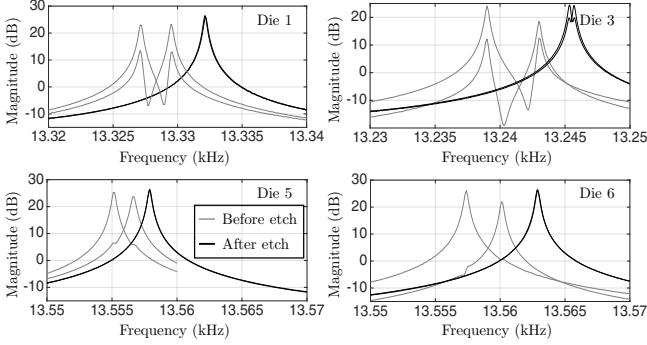| Die	ω_1 (Hz)	ω_2 (Hz)	Q_1 (k)	Q_2 (k)	Δ (Hz)
1	13332.12	13332.16	51.7	47.6	0.04
3	13245.40	13245.73	45.5	45.1	0.33
5	13557.81	13557.84	46.7	48.4	0.03
6	13562.83	13562.89	47.9	43.7	0.06
7	13234.18	13249.51	49.6	48.8	15.33
9	13617.82	13617.86	49.2	49.5	0.04
10	13596.72	13596.77	49.8	49.9	0.05
11	12984.00	12984.06	51.3	48.0	0.06
15	12946.57	12946.61	54.7	55.0	0.04

Fig. 8. Comparison of resonator frequency responses before and after the Parylene ablation-etch cycles for Die 1, 3, 5 and 6. The S_1/D_1 and S_2/D_2 channels are graphed for the resonators before and after the etch cycles.

Fig. 10. Summary for Die 5 after major etch steps. Both S_1/D_1 and S_2/D_2 channels are graphed after each major etch step.
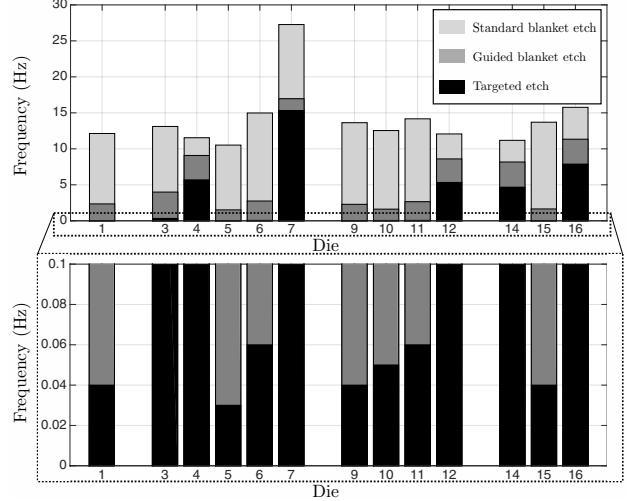
Fig. 11. Bar graph summarizing the $n = 2$ modal frequency differences for all die after the major etch steps.

differences to below the bandwidth of the resonances when starting from initial frequency differences of about 3 Hz or less. The guided blanket etch was an important step in realizing these starting values for the Parylene cycles. The challenge with the guided blanket etch, though, is the fact that the stiffness associated with the $n = 2$ modes is also clearly modified in addition to the mass distribution of the resonator. This is evident by comparing the data summarized in Tables II and III but is more clearly observed in Fig. 10, which shows the frequency response of Die 5 after the major etch steps, and Fig. 11, which shows a bar chart of the frequency differences for all die after the major etch steps. Note that the mean modal frequencies of the $n = 2$ modes *decrease* by a
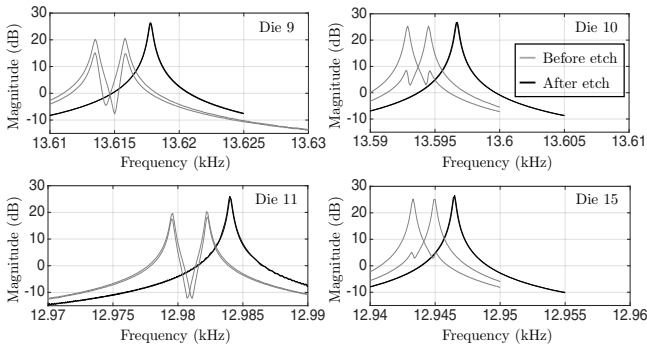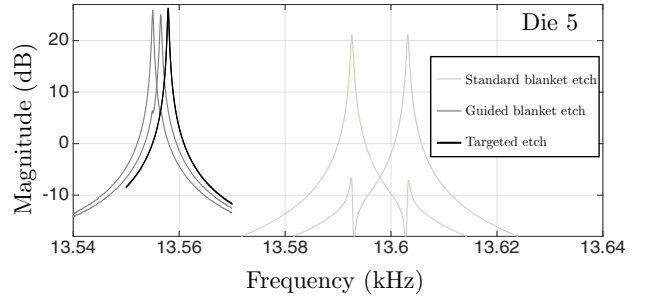

Fig. 9. Comparison of resonator frequency responses before and after the Parylene ablation-etch cycles for Die 9, 10, 11, and 15. The S_1/D_1 and S_2/D_2 channels are graphed for the resonators before and after the etch cycles.

significant amount by continuing the blanket etch. This fact – uncontrolled modification of the resonator stiffness – renders the guided blanket etch a useful tool but one that cannot be used to effectively eliminate the modal frequency difference. It is also interesting to note that the control die also experience a reduction in modal frequency difference during the guided blanket etch, although not to the extent of the die with ablated photoresist. Thus, it appears that after initial release of the resonators, continued etching reduces the modal frequency differences although in a largely unpredictable manner. The mechanism is attributed to continued lateral etching of the exposed resonator sidewalls, impacting both local stiffness and mass.

Performing a timed etch after deposition, and then ablation, of Parylene, produces highly repeatable and predictable results because the areas where the material removal occurs, i.e. the large spokes, has little impact on the $n = 2$ stiffness properties and so can be modeled as purely a perturbation to the resonator mass distribution. This was the basis of the perturbation model (9). Evidence of mass-only perturbations is also supported by Figs. 8 and 9 where it is clear that material removal uniformly increases the modal frequencies of the $n = 2$ modes. This demonstrates that the conformal Parylene coating is effective in preventing sidewall etching during the site-specific mass removal. Ideally, the compre-

TABLE VII
BOUNDS FOR Δ COMPUTED FROM (9)

Die	$\Delta_{\min}$ (Hz)	$\Delta_{\max}$ (Hz)
1	-0.36	0.07
3	-0.32	0.42
5	-0.03	0.31
6	0.05	0.41
7	15.35	15.52
9	0.05	0.27
10	-0.13	0.17
11	-0.15	0.37
15	0.07	0.26

hensive perturbation model (9) would be used to search for ablation sites, but due to the limited sensing of the outer ring radial motion, it is not possible to reliably estimate all of the parameters necessary for application of (9). In particular, the phases associated with the $k \in \{6, 10\}$ harmonics are not known. The analysis shows that the largest $k \in \{6, 10\}$ harmonic amplitudes are located in spoke layer $i = 1$ and have amplitudes that are approximately 4% and 3% of $k = 2$ harmonic amplitude. Thus, locating sense electrodes in this area of the resonator would be advantageous for measuring these phases. Nevertheless, bounds on Δ can be computed using (9) by searching for worst-case values of $\psi_{p,6}$ and $\psi_{p,10}$ where the relations $|\psi_{1,6} - \psi_{2,6}| = 15°$ and $|\psi_{1,10} - \psi_{2,10}| = 9°$ are assumed based on the finite element results. Profilometer measurements provide accurate estimates of the mass removal so the largest uncertainty in the parameters in (9) are the unknown phases. The bounds are shown in Table VII and are computed using accurate mass removal estimates starting from the resonator states after the guided blanket etch but before any targeted etching with the Parylene has occurred. The bounds demonstrate that Δ can significantly deviate from the final desired modal frequency difference of approximately zero. The real utility of the bounds is in showing the possible range of outcomes for Δ if only a single ablation-etch cycle is permitted in which the simplified model (11) is used to reduce Δ to approximately zero. The bounds imply that the absolute modal frequency difference may actually be as large as 0.4 Hz (excluding Die 7). These potentially large deviations were avoided by employing several ablation-etch cycles, thus, this method has been demonstrated to be compatible with iterative execution, enabling repeated application to achieve increasingly small frequency splits. Ultimately, however, a single ablation-etch cycle is most desirable, but this will necessitate the measurement of the unknown phases.

Finally, the quality factors are reported and appear to have experienced modest changes over the course of the experiments. In some cases the quality factors have increased and in others, they have decreased, but in general they appear to remain high throughout the post-fabrication steps.

V. CONCLUSION

A wafer-level post-fabrication technique has been demonstrated for simultaneous reduction of the modal frequency differences between the $n = 2$ modes in an axisymmetric resonator. The resonator is designed so that mass removal at the large spokes creates a readily predictable perturbation to its dynamics. Using a model-based approach to select these areas, a laser is used to ablate the masking resist and, subsequently, a conformal layer of Parylene-C, to expose the silicon for further etching with SiDRIE. The lateral dimensions can be tightly controlled with a fixed mask for the laser and the depth is controlled through a timed etch. Since only silicon is removed from the resonator, the process is compatible with any further processing, including wafer-level packaging operations.

REFERENCES

[1] D. Kim and R. M'Closkey, "Spectral analysis of vibratory gyro noise," *IEEE Sensors J.*, vol. 13, pp. 4361–4374, Nov. 2013.
[2] A. Challoner, H. Ge, and J. Liu, "Boeing disc resonator gyroscope," in *Proc. 2014 IEEE/ION Position, Location and Navigation Symp.*, Monterey, CA, May 2014, pp. 504–514.
[3] D. Schwartz, D. Kim, P. Stupar, J. DeNatale, and R. M'Closkey, "Modal parameter tuning of an axisymmetric resonator via mass perturbation," *J. Microelectromech. Syst.*, vol. 24, no. 3, pp. 545–555, June 2015.
[4] S. Nitzan, C. Ahn, T.-H. Su, M. Li, E. Ng, S. Wang, Z. Yang, G. O'Brien, B. Boser, T. Kenny, and D. Horsley, "Epitaxially-encapsulated polysilicon disk resonator gyroscope," in *Proc. IEEE MEMS*, Taipei, Jan. 2013, pp. 625–628.
[5] A. A. Trusov, I. P. Prikhodko, S. A. Zotov, and A. M. Shkel, "Low-dissipation silicon tuning fork gyroscopes for rate and whole angle measurements," *IEEE Sensors J.*, vol. 11, no. 11, pp. 2763–2770, Nov 2011.
[6] J. Bernstein, M. Bancu, E. Cook, M. Chaparala, W. Teynor, and M. Weinberg, "A MEMS diamond hemispherical resonator," *J. Micromech. Microeng.*, vol. 23, no. 12, pp. 1 – 8, Oct. 2013.
[7] J. Bernstein, M. Bancu, E. Cook, T. Henry, P. Kwok, T. Nyinjee, G. Perlin, W. Teynor, and M. Weinberg, "Diamond hemispherical resonator fabrication by isotropic glass etch," in *Proc. Solid-State Sensors, Actuators and Microsystems Workshop*, Hilton Head, SC, June 2014, pp. 273–276.
[8] P. Shao, C. Mayberry, X. Gao, V. Tavassoli, and F. Ayazi, "A polysilicon microhemispherical resonating gyroscope," *J. Microelectromech. Syst.*, vol. 23, pp. 762–764, Aug 2014.
[9] I. Prikhodko, S. Zotov, A. Trusov, and A. Shkel, "Microscale glass-blown three-dimensional spherical shell resonators," *J. Microelectromech. Sys.*, vol. 20, no. 3, pp. 691 – 701, June 2011.
[10] S. Zotov, A. Trusov, and A. Shkel, "Three-dimensional spherical shell resonator gyroscope fabricated using wafer-scale glassblowing," *J. Microelectromech. Syst.*, vol. 21, no. 3, pp. 509 – 510, June 2012.
[11] M. Kanik, P. Bordeenithikasem, D. Kim, N. Selden, A. Desai, R. M'Closkey, and J. Schroers, "Metallic glass hemispherical shell resonators," *J. Microelectromech. Syst.*, vol. 24, no. 1, pp. 19–28, Jan 2015.
[12] P. Taheri-Tehrani, T.-H. Su, A. Heidari, G. Jaramillo, C. Yang, S. Akhbari, H. Najar, S. Nitzan, D. Saito, L. Lin, and D. Horsley, "Microscale diamond hemispherical resonator gyroscope," in *Proc. Solid-State Sensors, Actuators and Microsystems Workshop*, Hilton Head, SC, June 2014, pp. 289 – 292.
[13] J. Y. Cho, J.-K. Woo, J. Yan, R. Peterson, and K. Najafi, "Fused-silica micro birdbath resonator gyroscope (μ-BRG)," *J. Microelectromech. Syst.*, vol. 23, no. 1, pp. 66 – 77, Feb 2014.
[14] R. Horning, B. Johnson, R. Compton, and E. Cabuz, "Hemitoroidal resonator gyroscope," U.S. Patent 8 631 702 B2, 2014.
[15] B. Gallacher, J. Hedley, J. Burdess, A. Harris, A. Rickard, and D. King, "Electrostatic correction of structural imperfections present in a microring gyroscope," *J. Microelectromech. Syst.*, vol. 14, pp. 221–234, April 2005.
[16] S. S. Rao, *Vibration of Continuous Systems*. Hoboken, NJ: John Wiley & Sons, 2007.
[17] C. Fox, "A simple theory for the analysis and correction of frequency splitting in slightly imperfect rings," *J. Sound Vib.*, vol. 142, no. 2, pp. 227–243, 1990.